PIER M

A SM-PB Acceleration Algorithm for Calculating Electromagnetic Scattering from 2D Gaussian Rough Surfaces

Shaoliang Yuan*

School of Big Data and Artificial Intelligence, Fujian Polytechnic Normal University, Fuzhou 350300, China

ABSTRACT: In this paper, an SM-PB (Sparse Matrix Canonical Grid method-Physics Based Two Grid) acceleration algorithm is proposed which can be used to calculate electromagnetic scattering from two-dimensional rough surfaces with large dielectric constants. Firstly, a two-dimensional rough surface model is established based on the Monte Carlo method and Gaussian spectral function, and a conical incident wave with Gaussian characteristics is introduced to eliminate the error caused by artificial truncation of the rough surface. In the scattering calculation, the integral equation of the rough surface is processed by the SMCG algorithm, and then the matrix equation is further processed by applying the PBTG algorithm to decompose the matrix equation into the very near-field matrix, near-field matrix, and far-field matrix. The FFT method is then used to calculate the matrix vector product during the iteration for fast computation. The proposed algorithm and MoM algorithm were compared from the perspectives of computational accuracy and efficiency. Through comparison, it was found that the two algorithms produced highly consistent results, validating the effectiveness of the proposed algorithm. The proposed algorithm demonstrated a significant advantage in computational efficiency, with considerable efficiency also observed for large-scale rough surfaces. The electromagnetic scattering from rough surfaces with large dielectric constants was calculated, and the influence of the correlation distance r_d and dielectric constant on the electromagnetic scattering characteristics was investigated. It was found that it is important to set a reasonable value of r_d in order to balance calculation accuracy and calculation efficiency.

1. INTRODUCTION

After the Second World War, radar technology has been developed rapidly. In terms of social livelihood, the electromagnetic waves emitted by radar generate environmental scattering [1–7] echoes when they irradiate to the ground and sea surface, which contain rich surface information of ground and sea surface environment, such as soil type, water content, soil surface undulation degree, sea surface wind speed, and dielectric constant of seawater. This information can be used for land resource survey, ecological environment monitoring, agricultural monitoring and crop yield estimation, disaster forecasting and disaster assessment, marine environment survey, etc. Even in daily life, weather forecasting and air quality monitoring involve the study of environmental scattering properties, which can be useful in disaster prevention and mitigation and meteorological and geological disaster monitoring. In the military field, ambient electromagnetic scattering characteristics are the key to technologies such as radar remote sensing detection [8–13] and radar image processing [14–18]. Electromagnetic waves emitted by radar are commonly used to detect and track targets hidden in the ground and sea surface environment. Since the target is in various complex natural environments, when the radar-emitted electromagnetic wave irradiates to the target and also irradiates to the environmental background, the scattered echo contains the useful signal scattered back from the target and the clutter signal scattered back from the natural environment, and the target signal will be drowned in the environmental clutter, which will seriously affect the detection and identification of the target signal by the radar signal processing system and eventually lead to the target cannot be found. In conclusion, the environmental scattering characteristics and its clutter characteristics should be studied in detail, both in military and civil applications.

In the development of computational methods, there are mainly four descriptive approaches for solving the mathematical model of rough surface scattering: frequency domain differential equations (FDDE), time domain differential equations (TDDE), frequency domain integral equations (FDIE), and time domain integral equations (TDIE). The classical method based on FDDE is the finite element method (FEM) [19]. This method is based on variational principles and transforms the desired boundary value problem into an appropriate variational problem, which is then converted into a general multiple function extremum problem through discretization. Finally, the numerical solution of the boundary value problem is obtained by solving an algebraic equation system.

The most typical numerical algorithm based on TDDE is finite difference time domain method (FDTD) [20]. This method was first proposed by Yee [21] in 1966. As it directly solves the time domain Maxwell equations, it can not only calculate scattering excited by time-harmonic field sources, but also calculate scattering excited by pulse wave sources. One of the more widely used numerical methods based on frequency domain integral equations (FDIE) is the method of moments (MoM). This method was proposed by Harrington [22], and its basic idea is to first choose suitable integral equations for the electric field or

* Corresponding author: Shaoliang Yuan (sly_fpnu@126.com).

magnetic field, then expand the unknown quantities using expansion functions, and finally perform the inner product on both sides of the integral equation using weight functions, which transforms the integral equation into an algebraic equation for solution.

In researching computational backgrounds, Dölz [23] proposed a higher order perturbation approach for solving the time-harmonic electromagnetic scattering problems on a perfectly conducting scatterer with uncertain shape and gave an efficient solution for its discretization and boundary integral equation solution by three examples. However, this algorithm is not able to perform an efficient calculation of the scattering from the medium. Ozgun et al. [24] proposed a novel computational electromagnetics (CEM) technique, which is based on the periodic finite element method (FEM) with the method of moments (MoM) and has unique advantages in computing large truncated metasurfaces involving arbitrarily inhomogeneous unit cells, but it is not widely applicable because the method requires high-order moment and high-order basis function calculations, resulting in relatively low computational efficiency and high requirements for computer performance. He et al. [25] developed a multi-stage fast multipole method (MLFMM) algorithm model to study the electromagnetic scattering characteristics of camouflaged grass in different frequency bands. In order to make the electromagnetic properties of camouflage grass resemble natural grass as much as possible, he compared the calculated results with the measured ones several times and continuously improved the accuracy of the model, discussing the effects of blade length, width, and density on the electromagnetic scattering characteristics. His results can be used for military camouflage to improve the electromagnetic "stealth" performance of one's equipment from enemy detection, thus improving military strike capability and survivability. In fact, stealth and anti-stealth has been a topic of widespread concern, and the study of environmental electromagnetic scattering characteristics can not only improve the stealth capability of one's own weapons and equipment and increase concealment but also facilitate the identification and detection of enemy equipment, so that the enemy cannot hide anything. Therefore, it is important to study the electromagnetic scattering properties of the environment from several perspectives, and a good algorithm is the key to effective research, which is related to the accuracy and practicality of the study.

In this paper, an accelerated SM-PB algorithm is proposed for calculating two-dimensional dielectric rough surfaces with large dielectric constants, which first processes the surface integral equation with the SMCG algorithm and then combines it with the PBTG algorithm to accelerate the calculation. During the processing, the matrix equation is decomposed as: (1) Very near-field matrix: The correlation distance is less than half a wavelength, and the matrix vector product is done directly. (2) Near-field matrix: The correlation distance is greater than half a wavelength and less than the strong and weak correlation distances, and the free-space surface electromagnetic field is the average of the dielectric space surface electromagnetic field. Then, the matrix vector product is performed. (3) Far-field matrix: The correlation distance is greater than the strong and weak correlation distance, and the Taylor series expansion is

performed on the free-space Green's function. Then the matrix vector is calculated by applying FFT, and its properties in the iterative method are used to calculate the matrix vector product quickly respectively, thus speeding up the computation. The algorithm requires an amount of memory of $O(N)$ and a computation time of $O(N \log(N))$. The accuracy and practicality of the algorithm are demonstrated by algorithm validation. Finally, the electromagnetic scattering characteristics at different r_d are calculated, and the effect of the dielectric constant on the ambient electromagnetic scattering is discussed.

2. GAUSSIAN ROUGH SURFACE AND CONICAL INCIDENT WAVE

2.1. Gaussian Rough Surface

The ground environment in nature usually has different shape characteristics. Before analyzing the electromagnetic scattering characteristics of the ground environment, Monte Carlo method combined with Gaussian spectral function is first used to establish a two-dimensional ground environment geometric model.

The height profile function of the rough surface is [26]:

$$f(x, y) = \frac{1}{L_x L_y} \sum_{m=-\infty}^{\infty} \sum_{n=-\infty}^{\infty} b_{mn}$$

$$\exp\left(\frac{j2\pi mx}{L_x}\right) \exp\left(\frac{j2\pi ny}{L_y}\right) \quad (1)$$

where the Gaussian spectral functions $W(K_m, K_n)$ and coefficients of the 2D Gaussian rough surface are:

$$b_{mn} = 2\pi \sqrt{L_x L_y W(K_{xm}, K_{yn})}$$

$$\begin{cases} \frac{N(0,1)+jN(0,1)}{\sqrt{2}} & m \neq 0, \ N_x/2, n \neq 0, N_y/2 \\ N(0,1) & m = 0, \ N_x/2 \ or \ n = 0, N_y/2 \end{cases} \quad (2)$$

$$W(K_x, K_y) = \frac{l_x l_y h^2}{4\pi} \exp\left(-\frac{K_x^2 l_x^2}{4} - \frac{K_y^2 l_y^2}{4}\right) \quad (3)$$

where l_x and l_y are the correlation lengths in the x and y directions, respectively; h is the root mean square height; K_{xm} and K_{yn} are the discrete points of the spatial frequencies in the x and y directions, respectively; L_x and L_y are the contour lengths of the rough surface in the x and y directions.

In the above equation, $N(0, 1)$ is a sampling point in a random sequence that satisfies a normal distribution with mean 0. The rest of the parameters are labeled in detail in [26] and are not repeated here.

It is worth noting that the coefficient b_{mn} must be conjugately symmetric about the origin for the surface height values to be real, so there is:

$$b(m, n) = b^*(-m, -n)$$
$$b(m, -n) = b^*(-m, n) \quad (4)$$

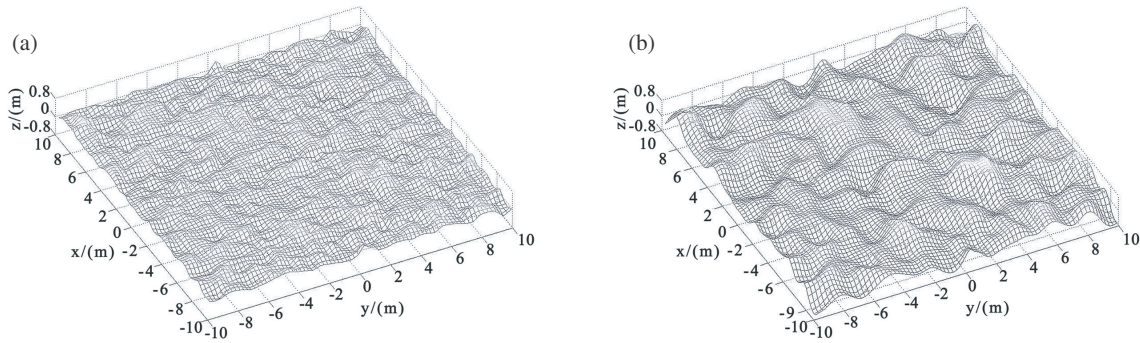**FIGURE 1**. Two-dimensional Gaussian rough surfaces. (a) $h = 0.1\,\text{m}$, $l_x = l_y = 0.5\,\text{m}$, $L_x \times L_y = 20 \times 20\,(\text{m}^2)$. (b) $h = 0.3\,\text{m}$, $l_x = l_y = 1.0\,\text{m}$, $L_x \times L_y = 20 \times 20\,(\text{m}^2)$.

By further derivation, the partial derivative equation of $f(x, y)$ with respect to x and y can be obtained:

$$f'_x(x_m, y_n) = \frac{1}{L_x L_y} \sum_{p=-\frac{N_x}{2}+1}^{\frac{N_x}{2}} \sum_{q=-\frac{N_y}{2}+1}^{\frac{N_y}{2}} b_{mn} \left(\frac{j2\pi p}{L_x} \right)$$

$$\exp\left(\frac{j2\pi p x_m}{L_x} \right) \exp\left(\frac{j2\pi q y_n}{L_y} \right) \tag{5}$$

$$f'_y(x_m, y_n) = \frac{1}{L_x L_y} \sum_{p=-\frac{N_x}{2}+1}^{\frac{N_x}{2}} \sum_{q=-\frac{N_y}{2}+1}^{\frac{N_y}{2}} b_{mn} \left(\frac{j2\pi q}{L_y} \right)$$

$$\exp\left(\frac{j2\pi p x_m}{L_x} \right) \exp\left(\frac{j2\pi q y_n}{L_y} \right) \tag{6}$$

They are all in two-dimensional DFT form, so they can be solved by the two-dimensional FFT algorithm to improve computational efficiency. Fig. 1 shows the generated rough surfaces for different parameters.

2.2. Conical Incident Wave

In the actual rough surface scattering, since the simulation generates a finite rough surface, the electromagnetic wave will produce a bypassing phenomenon at the edge of the rough surface, leading to errors in the calculation results. In order to reduce this error, the incident wave is treated in a certain way to make it a 'conical wave' [27]. The essence of a conical wave is to add a modulation window function to an infinite plane wave so that the incident wave intensity at the edge tends to zero. Radar irradiation waves are also in the shape of a beam, and the use of conical waves can simulate the actual situation to a certain extent and has engineering significance.

The incident wave vector can be expressed as:

$$\mathbf{k}_i = \sin\theta_i \cos\phi_i \mathbf{x} + \sin\theta_i \sin\phi_i \mathbf{y} - \cos\theta_i \mathbf{z} \tag{7}$$

where θ_i is the incident vertical angle, and ϕ_i is the azimuthal angle.

For TE incident waves, the EM equation is:

$$\mathbf{E}_{inc}(\mathbf{r}) = \int_{-\infty}^{+\infty} \int_{-\infty}^{+\infty} \exp\left(jk_x x + jk_y y - jk_z z \right)$$

$$\cdot E(k_x, k_y) \mathbf{h}_i(-k_z) \, dk_x dk_y \tag{8}$$

$$\mathbf{H}_{inc}(\mathbf{r}) = -\frac{1}{\eta_0} \int_{-\infty}^{+\infty} \int_{-\infty}^{+\infty} \exp\left(jk_x x + jk_y y - jk_z z \right)$$

$$\cdot E(k_x, k_y) \mathbf{v}_i(-k_z) \, dk_x dk_y \tag{9}$$

For TM incident waves, the EM equation is:

$$\mathbf{E}_{inc}(\mathbf{r}) = \int_{-\infty}^{+\infty} \int_{-\infty}^{+\infty} \exp\left(jk_x x + jk_y y - jk_z z \right)$$

$$\cdot E(k_x, k_y) \mathbf{v}_i(-k_z) \, dk_x dk_y \tag{10}$$

$$\mathbf{H}_{inc}(\mathbf{r}) = -\frac{1}{\eta_0} \int_{-\infty}^{+\infty} \int_{-\infty}^{+\infty} \exp\left(jk_x x + jk_y y - jk_z z \right)$$

$$\cdot E(k_x, k_y) \mathbf{h}_i(-k_z) \, dk_x dk_y \tag{11}$$

In the above equation, $\mathbf{h}_i$ is the horizontal polarization direction; $\mathbf{v}_i$ is the vertical polarization direction; η_0 is the free space wave impedance; k_x, k_y, and k_z are the spatial spectrum in the x, y, and z directions, respectively.

$E(k_x, k_y)$ is the spectrum of the incident wave:

$$E(k_x, k_y) = \frac{1}{4\pi^2} \int_{-\infty}^{+\infty} dx \int_{-\infty}^{+\infty} \exp\left(-jk_x x - jk_y y \right)$$

$$\cdot \exp\left(j(k_{ix} x + k_{iy} y)(1 + w) \right) \exp(-t) \, dy \tag{12}$$

where

$$t = t_x + t_y = \left(x^2 + y^2 \right)/g^2 \tag{13}$$

$$t_x = \frac{(\cos\theta_i \cos\phi_i x + \cos\theta_i \sin\phi_i y)^2}{g^2 \cos^2\theta_i} \tag{14}$$

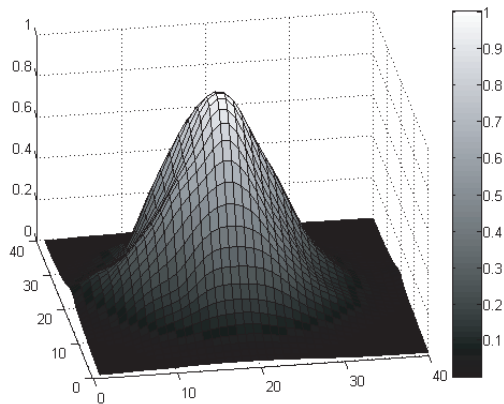$$t_y = \frac{(-\sin\phi_i x + \cos\phi_i y)^2}{g^2} \tag{15}$$

FIGURE 2. Normalized conical wave schematic.

FIGURE 3. Schematic diagram of incident.

$$w = \frac{1}{k_0^2}\left[\frac{(2t_x - 1)}{g^2 \cos^2\theta_i} + \frac{(2t_y - 1)}{g^2}\right] \tag{16}$$

The value of the beamwidth g determines the intensity of the incident wave irradiation, and a reasonable result can be obtained when it satisfies the following relationship:

$$g \geq \frac{6}{(\cos\theta_i)^{1.5}}, \quad L = 4g \tag{17}$$

When $\theta_i = 60°$, $\varphi_i = 0°$, the two-dimensional normalized conical incident wave amplitude is shown in Fig. 2.

3. ELECTROMAGNETIC SCATTERING MODEL AND ALGORITHM VALIDATION

3.1. Surface Integral Equation

The expression of the integral equation for the rough surface of a two-dimensional medium is given by:

$$\mathbf{n}\cdot\mathbf{E}_{inc}(\mathbf{r}) = \frac{\mathbf{n}\cdot\mathbf{E}(\mathbf{r})}{2} - \mathbf{n}\cdot\left\{\int_{S_r} j\omega\mu_0 \mathbf{n}'\times\mathbf{H}(\mathbf{r}')g_0(\mathbf{r},\mathbf{r}')ds'\right.$$

$$+ P\int_{S_r}[(\mathbf{n}'\times\mathbf{E}(\mathbf{r}'))\times\nabla'g_0(\mathbf{r},\mathbf{r}')$$

$$+ \nabla'g_0(\mathbf{r},\mathbf{r}')\mathbf{n}'\cdot\mathbf{E}(\mathbf{r}')]ds'\} \tag{18}$$

$$\mathbf{n}\times\mathbf{H}_{inc}(\mathbf{r}) = \frac{\mathbf{n}\times\mathbf{H}(\mathbf{r})}{2} + \mathbf{n}\times\left\{\int_{S_r} j\omega\varepsilon_0\mathbf{n}'\times\mathbf{E}(\mathbf{r}')g_0(\mathbf{r},\mathbf{r}')ds'\right.$$

$$- P\int_{S_r}[\nabla'g_0(\mathbf{r},\mathbf{r}')\mathbf{n}'\cdot\mathbf{H}(\mathbf{r}')$$

$$+ \int_{S_r}(\mathbf{n}'\times\mathbf{H}(\mathbf{r}'))\times\nabla'g_0(\mathbf{r},\mathbf{r}')\Big]ds'\} \tag{19}$$

$$0 = -\frac{\mathbf{n}\times\mathbf{E}(\mathbf{r})}{2} - \mathbf{n}\times\left\{\int_{S_r} j\omega\mu_1\mathbf{n}'\times\mathbf{H}(\mathbf{r}')g_1(\mathbf{r},\mathbf{r}')ds'\right.$$

$$+ P\int_{S_r}[(\mathbf{n}'\times\mathbf{E}(\mathbf{r}'))\times\nabla'g_1(\mathbf{r},\mathbf{r}')$$

$$+ \nabla'g_1(\mathbf{r},\mathbf{r}')\frac{\varepsilon_0}{\varepsilon_1}\mathbf{n}'\cdot\mathbf{E}(\mathbf{r}')\Big]ds'\} \tag{20}$$

$$0 = -\frac{\mathbf{n}\cdot\mathbf{H}(\mathbf{r})}{2} + \mathbf{n}\cdot\left\{\int_{S_r} j\omega\varepsilon_1\mathbf{n}'\times\mathbf{E}(\mathbf{r}')g_1(\mathbf{r},\mathbf{r}')ds'\right.$$

$$- P\int_{S_r}\left[\nabla'g_1(\mathbf{r},\mathbf{r}')\frac{\mu_0}{\mu_1}\mathbf{n}'\cdot\mathbf{H}(\mathbf{r}')\right.$$

$$+ (\mathbf{n}'\times\mathbf{H}(\mathbf{r}'))\times\nabla'g_1(\mathbf{r},\mathbf{r}')]ds'\} \tag{21}$$

Expanding the above four equations with each vector direction, we can obtain six scalar surface integral equations. To save the space of the article, three of these equations are listed in this subsection, and the remaining equations can be derived using the same procedure.

$$F_x^{inc}(\mathbf{r}) = \frac{F_x(\mathbf{r})}{2} + \iint\left\{-j\frac{k_0}{\eta_0}g_0 I_x(\mathbf{r}')\left[\frac{\partial f(x,y)}{\partial y}\frac{\partial f(x',y')}{\partial x'}\right]\right.$$

$$-j\frac{k_0}{\eta_0}g_0 I_y(\mathbf{r}')\left(\frac{\partial f(x,y)}{\partial y}\frac{\partial f(x',y')}{\partial y'}+1\right)\Big\}dx'dy'$$

$$+ \iint\left\{G_0(R)F_x(\mathbf{r}')\left[\frac{\partial f(x,y)}{\partial y}(y-y')\right.\right.$$

$$+ \frac{\partial f(x',y')}{\partial x'}(x-x')-(z-z')\Big]$$

$$+ G_0(R)F_y(\mathbf{r}')\left[-\frac{\partial f(x,y)}{\partial y}(x-x')\right.$$

$$+ \frac{\partial f(x',y')}{\partial y'}(x-x')\Big]$$

$$+ G_0(R)F_n(\mathbf{r}')\left[\frac{\partial f(x,y)}{\partial y}(z-z')\right.$$

$$+ (y-y')]\}dx'dy' \tag{22}$$

$$F_y^{inc}(\mathbf{r}) = \frac{F_y(\mathbf{r})}{2} + \iint\left\{-j\frac{k_0}{\eta_0}g_0 I_x(\mathbf{r}')\left[-1-\frac{\partial f(x',y')}{\partial x'}\frac{\partial f(x,y)}{\partial x}\right]\right.$$

$$+j\frac{k_0}{\eta_0}g_0 I_y\left(\mathbf{r}'\right)\frac{\partial f\left(x,y\right)}{\partial y}\frac{\partial f\left(x,y\right)}{\partial x}\bigg\}\,dx'dy'$$

$$+\iint\bigg\{G_0\left(R\right)F_x\left(\mathbf{r}'\right)\left[\frac{\partial f\left(x',y'\right)}{\partial x'}\left(y-y'\right)\right.$$

$$\left.-\frac{\partial f\left(x,y\right)}{\partial x}\left(y-y'\right)\right]$$

$$+G_0\left(R\right)F_y\left(\mathbf{r}'\right)\left[-\left(z-z'\right)\right.$$

$$\left.+\frac{\partial f\left(x',y'\right)}{\partial y'}\left(y-y'\right)+\frac{\partial f\left(x,y\right)}{\partial x}\left(x-x'\right)\right]$$

$$+G_0\left(R\right)F_n\left(\mathbf{r}'\right)\left[-\frac{\partial f\left(x,y\right)}{\partial x}\left(z-z'\right)\right.$$

$$\left.-\left(x-x'\right)\right]\bigg\}\,dx'dy' \tag{23}$$

$$I_n^{inc}\left(\mathbf{r}\right)=\frac{I_n\left(\mathbf{r}\right)}{2}+\iint\bigg\{G_0(R)I_x(\mathbf{r}')\left[-\frac{\partial f(x,y)}{\partial x}\frac{\partial f(x',y')}{\partial x'}(y-y')\right.$$

$$+\frac{\partial f(x,y)}{\partial y}\left[\frac{\partial f(x',y')}{\partial x'}(x-x')-(z-z')\right]-(y-y')\bigg]$$

$$+G_0\left(R\right)I_y\left(\mathbf{r}'\right)\left[\frac{\partial f\left(x,y\right)}{\partial x}\left[(z-z')\right.\right.$$

$$\left.+\frac{\partial f\left(x',y'\right)}{\partial y'}\left(y-y'\right)\right]$$

$$\left.+\frac{\partial f\left(x,y\right)}{\partial y}\frac{\partial f\left(x',y'\right)}{\partial y'}\left(x-x'\right)+\left(x-x'\right)\right]$$

$$+G_0\left(R\right)I_n\left(\mathbf{r}'\right)\left[\frac{\partial f\left(x,y\right)}{\partial x}\left(x-x'\right)\right.$$

$$\left.+\frac{\partial f\left(x,y\right)}{\partial y}\left(y-y'\right)-\left(z-z'\right)\right]\bigg\}\,dx'dy'$$

$$+\iint\bigg\{jk_0\eta_0 g_1 F_x(\mathbf{r}')\left[\frac{\partial f(x,y)}{\partial x}-\frac{\partial f(x',y')}{\partial x'}\right]$$

$$+jk_0\eta_0 g_0 F_y(\mathbf{r}')\left[\frac{\partial f(x,y)}{\partial y}-\frac{\partial f(x',y')}{\partial y'}\right]\bigg\}\,dx'dy' \tag{24}$$

The dielectric constant and permeability of medium 1 and medium 2 are $\varepsilon_{1,2}$ and $\mu_{1,2}$. $\mathbf{E}_{1,2}(\mathbf{r})$ and $\mathbf{H}_{1,2}(\mathbf{r})$ are the electromagnetic fields of mediums 1 and 2, respectively; g_1 and g_2 are the Green's functions of mediums 1 and 2; η_1 and η_2 are the wave impedances of mediums 1 and 2. Then:

$$g_{1,2}=\frac{\exp\left(jk_{1,2}R\right)}{4\pi R} \tag{25}$$

$$\nabla' g_{1,2}=\left(\mathbf{r}-\mathbf{r}'\right)G_{1,2}\left(R\right) \tag{26}$$

$$G_{1,2}\left(R\right)=\frac{\left(1-jk_{1,2}R\right)\exp\left(jk_{1,2}R\right)}{4\pi R^3} \tag{27}$$

In the MoM solution process, it is necessary to discretize the above six scalar surface integral equations into matrix equations:

$$\sum_{n=1}^{N}\sum_{q=1}^{6}Z_{mn}^{pq}I_n^{(q)}=I_m^{(p)inc} \tag{28}$$

where N is the number of discrete points, and Z_{mn}^{pq} is the impedance matrix.

At this point, if the matrix is solved directly, the number of unknowns can reach tens of thousands, and the computational efficiency is very low, which is unacceptable in practical use; for this reason, a suitable method is needed to accelerate the computational process. To solve this problem, the SM-PB acceleration algorithm is introduced next.

3.2. SM-PB Acceleration Algorithm

In the calculation process, the SMCG algorithm is first applied to the surface integral equation, and the obtained results are then processed by the PBTG algorithm, which can decompose the original matrix equation into the extreme near-field matrix, near-field matrix, and far-field matrix, then their properties in the iterative method to calculate the matrix vector product quickly, respectively, so as to achieve the purpose of accelerating the calculation.

Firstly, as shown in Fig. 3, introduce the strong and weak correlation distance r_d, which is determined by the topography of the scattering surface, to distinguish the near field from the far field. For example, the distance between two points on a rough surface is ρ_R. When $\rho_R > r_d$, it is considered as near field; when $\rho_R < r_d$, it is considered as far field. Therefore, the surface integral equations in the SMCG algorithm become:

$$\left(\mathbf{Z}^{(s)}+\mathbf{Z}^{(FS)}\right)\mathbf{X}^{(n+1)}=\mathbf{b}-\mathbf{Z}^{(w)}\mathbf{X}^{(n)} \tag{29}$$

where $\mathbf{Z}^{(s)}$ represents the near-field strong correlation matrix, $\mathbf{Z}^{(w)}$ the far-field weak correlation matrix, and $\mathbf{Z}^{(FS)}=\mathbf{Z}_0^{(w)}$ the planar matrix.

Applying Taylor series to extend $\mathbf{Z}^{(w)}$ to order M, then:

$$\mathbf{Z}^{(w)}=\sum_{m=0}^{M}\mathbf{Z}_m^{(w)} \tag{30}$$

Applying the Taylor series expansion to the Green's function in $\mathbf{Z}^{(w)}$ as well, the expression is as follows:

$$G_{1,2}\left(R\right)=\frac{\left(1-jk_{1,2}R\right)\exp\left(jk_{1,2}R\right)}{4\pi R^3}$$

$$=\sum_{m=0}^{M}a_m^{(1,2)}\left(\rho_R\right)\left(\frac{z_d^2}{\rho_R^2}\right)^m \tag{31}$$

$$g_{1,2}=\frac{\exp\left(jk_{1,2}R\right)}{4\pi R}=\sum_{m=0}^{M}b_m^{(1,2)}(\rho_R)\left(\frac{z_d^2}{\rho_R^2}\right)^m \tag{32}$$

$$z_d=f\left(x,y\right)-f\left(x',y'\right) \tag{33}$$

The first 3 orders of expansion are listed below:

$$a_0^{(1,2)} = \frac{1}{0!} \frac{\exp(jk_{1,2}\rho_R)}{4\pi\rho_R} \left(\frac{1}{\rho_R^2} - \frac{jk_{1,2}}{\rho_R} \right) \tag{34}$$

$$a_1^{(1,2)}(\rho_R) = \frac{1}{1!} \frac{\exp(jk_{1,2}\rho_R)}{4\pi\rho_R} \left[-\frac{k^2}{2} - \frac{3jk}{2\rho_R} + \frac{3}{2\rho_R^2} \right] \tag{35}$$

$$a_2^{(1,2)}(\rho_R) = \frac{1}{2!1!} \frac{\exp(jk_{1,2}\rho_R)}{4\pi\rho_R}$$

$$\left[-\frac{jk^3\rho_R}{4} + \frac{6k^2}{4} + \frac{15jk}{4\rho_R} - \frac{15}{4\rho_R^2} \right] \tag{36}$$

$$\cdots\cdots\cdots\cdots\cdots\cdots$$

$$b_0^{(1,2)} = \frac{1}{0!} \frac{\exp(jk_{1,2}\rho_R)}{4\pi\rho_R} \tag{37}$$

$$b_1^{(1,2)} = \frac{1}{1!} \frac{\exp(jk\rho_R)}{4\pi\rho_R} \left(\frac{jk\rho_R}{2} - \frac{1}{2} \right) \tag{38}$$

$$b_2^{(1,2)} = \frac{1}{2!1!} \frac{\exp(jk\rho_R)}{4\pi\rho_R} \left(-\frac{k^2\rho_R^2}{4} - \frac{3jk\rho_R}{4} + \frac{3}{4} \right) \tag{39}$$

$$\cdots\cdots\cdots\cdots\cdots$$

The iterative formula for the matrix equation is:

$$\left(\mathbf{Z}^{(s)} + \mathbf{Z}^{(FS)} \right) \mathbf{x}^{(1)} = \mathbf{b}_{inc} \tag{40}$$

$$\left(\mathbf{Z}^{(s)} + \mathbf{Z}^{(FS)} \right) \mathbf{x}^{(n+1)} = \mathbf{b}_{inc}^{(n+1)} \tag{41}$$

During the iteration, both $\mathbf{Z}^{(FS)}$ and $\mathbf{Z}^{(w)}$ can be decomposed into the form of a sum of planar C matrices, so they can be accelerated with the 2D-FFT algorithm. At the end of the iteration, $\sqrt{\left\| \mathbf{b}_{inc}^{(n)} \right\| / \|\mathbf{b}_{inc}\|} \times 100\% < \sigma$.

Based on the SMCG algorithm, the matrix equation is further processed by applying PBTG to decompose the matrix equation into the rough surface matrix of the lossy medium, the far-field matrix of the free-space rough surface, and the near-field matrix of the free-space rough surface.

In the solution process, sparse dissection is used in free space and dense dissection is used in medium space. The sparse profile is typically 10 nodes per wavelength, and the dense profile is typically 20 nodes per wavelength or more. Then, according to the decaying nature of the Green's function in lossy media and the slow variability of the Green's function on a large grid, the original matrix is changed into a sparse band matrix, and then the matrix equations are solved by an iterative method.

For dielectric rough surfaces, the loss of the Green's function is also large due to the large imaginary part of the dielectric constant. Therefore, the boundary distance r_l can be defined as:

$$r_l = \frac{C}{k_2''} \tag{42}$$

where k_2'' is the imaginary part of the wave number k_2 in the medium space, and C is a constant. When the distance between two nodes of a rough surface $r > r_l$, the interaction between these two nodes is weak, and the impedance matrix can be considered as zero. Therefore, the impedance matrix of the rough surface in dielectric space can be approximated as:

$$\mathbf{Z}_{mn}^{pq} = \tilde{\mathbf{Z}}_{mn}^{pq} = \begin{cases} \mathbf{Z}_{mn}^{pq} & r_{mn} \leq r_l \\ 0 & r_{mn} \geq r_l \end{cases} \tag{43}$$

r_{mn} denotes the distance between nodes m and n. As a result, the matrix equation of the rough surface of the medium space becomes:

$$\sum_{n=1}^{N_{sdg}} \sum_{q=1}^{6} \tilde{\mathbf{Z}}_{mn}^{pq} I_n^{(q)} = I_m^{(p)inc} \tag{44}$$

where sdg denotes the Single Dense Grid; N_{sdg} denotes the total number of nodes of Single Dense Grid; and $\tilde{\mathbf{Z}}_{mn}^{pq}$ denotes the sparse band matrix.

For the far-field matrix of a free space rough surface, the field values on the nodes of a sparse profile can be obtained by averaging over a large grid due to the slow variation of the Green's function at the nodes. Then, it is multiplied with the impedance matrix of the sparse profiling nodes to obtain the far-field matrix as:

$$\sum_{l=1}^{n_2^2} \mathbf{Z}_{(m+l)(n+l)}^{pq} I_{n+l}^{(q)} \approx \mathbf{Z}_{m_{mp}n_{mp}}^{pq} \sum_{l=1}^{n_2^2} I_{n+l}^{(q)}$$

$$= n_2^2 \mathbf{Z}_{m_{mp}n_{mp}}^{pq} \left(\frac{1}{n_2^2} \sum_{l=1}^{n_2^2} I_{n+l}^{(q)} \right) \tag{45}$$

where $l = 1, 2, \ldots, n_2^2$, and m_{mp}, n_{mp} denote the central nodes of $m+1, m+2, \ldots, m+n_2^2, n+1, n+2, \ldots, n+n_2^2$ respectively.

For the near-field matrix of a free space rough surface, a boundary distance r_f can also be defined, which is considered as near-field when $r < r_f$ and far-field when $r > r_f$. Then the matrix equation can be decomposed into the sum of the near-field matrix and far-field matrix, as follows:

$$\sum_{n=1}^{N_{sdg}} \mathbf{Z}_{mn}^{pq} I_n^{(q)} = \sum_{n=1}^{N_{sdg}} \mathbf{Z}_{mn}^{pq(s)} I_n^{(q)} + \sum_{n=1}^{N_{sdg}} \mathbf{Z}_{mn}^{pq(ns)} I_n^{(q)} \tag{46}$$

where the far-field matrix $\mathbf{Z}_{mn}^{pq(ns)}$ and the near-field matrix $\mathbf{Z}_{mn}^{pq(s)}$ are defined as:

$$\mathbf{Z}_{mn}^{pq(s)} = \begin{cases} \mathbf{Z}_{mn}^{pq} & r_{mn} \leq r_f \\ 0 & r_{mn} \geq r_f \end{cases} \tag{47}$$

$$\mathbf{Z}_{mn}^{pq(ns)} = \begin{cases} 0 & r_{mn} \leq r_f \\ \mathbf{Z}_{mn}^{pq} & r_{mn} \geq r_f \end{cases} \tag{48}$$

The matrix equation can then be transformed into a combination of densely profiled nodes and sparsely profiled nodes of
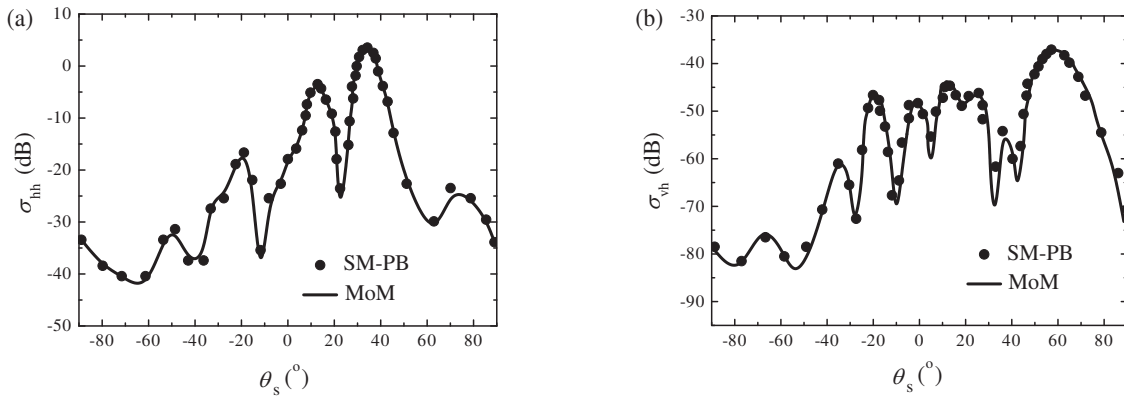
FIGURE 4. Validation of Algorithm. (a) hh polarization. (b) vh polarization.
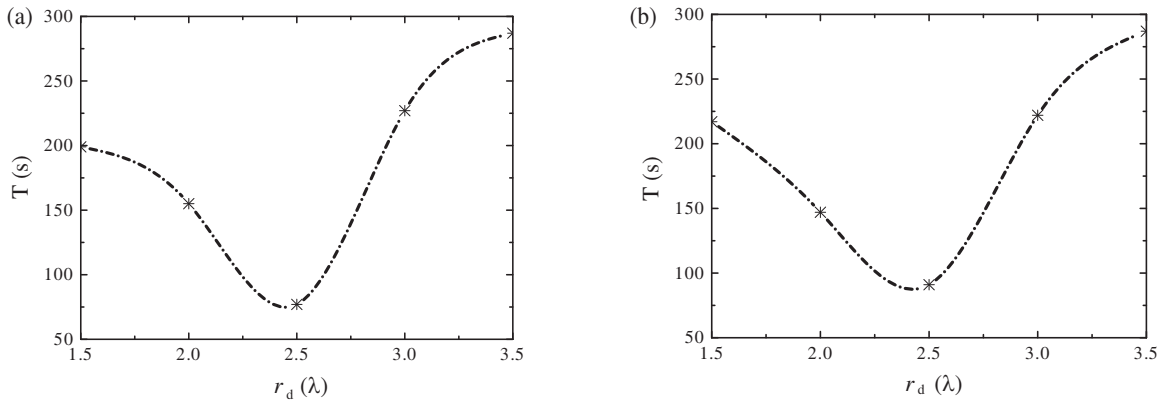

FIGURE 5. The variation curve of simulation time with r_d. (a) TE incident wave. (b) TM incident wave.

the following form:

$$\sum_{q=1}^{6}\sum_{n=1}^{N_{sdg}}\mathbf{Z}_{mn}^{pq(s)}I_n^{(q)} + \sum_{q=1}^{6}\left[\sum_{\tilde{n}=1}^{N_{scg}}\tilde{\mathbf{Z}}_{\tilde{m}\tilde{n}}^{pq(ns)}\tilde{I}_{\tilde{n}}^{(q)}\right]_{intp} = I_m^{(p)inc}$$

(49)

In the calculation, the field values on the sparsely profiled nodes are first calculated, and then linear interpolation is applied to find the field values on the densely profiled nodes.

Finally, the polarized bistatic scattering coefficients for rough surfaces can be derived as follows.

$$\varepsilon_h^s = \frac{jk_1}{4\pi}\int\exp\left(-jk_1\beta'\right)\left[\{I_x\left(x',y'\right)\cos\theta_s\cos\phi_s\right.$$

$$+I_y\left(x',y'\right)\cos\theta_s\sin\phi_s$$

$$-I_x\left(x',y'\right)\frac{\partial f\left(x',y'\right)}{\partial x'}\sin\theta_s$$

$$\left.-I_y\left(x',y'\right)\frac{\partial f\left(x',y'\right)}{\partial y'}\sin\theta_s\right\}$$

$$-\eta_1\{F_x(x',y')\sin\phi_s - F_y(x',y')\cos\phi_s\}]dx'dy' \quad (50)$$

$$\varepsilon_v^s = \frac{jk_1}{4\pi}\int\exp(-jk_1\beta')[\{I_x(x',y')\sin\phi_s - I_y(x',y')\cos\phi_s\}$$

$$+\eta_1\left\{F_x\left(x',y'\right)\cos\theta_s\cos\phi_s + F_y\left(x',y'\right)\cos\theta_s\sin\phi_s\right.$$

$$-F_x\left(x',y'\right)\frac{\partial f\left(x',y'\right)}{\partial x'}\sin\theta_s$$

$$\left.\left.-F_y\left(x',y'\right)\frac{\partial f\left(x',y'\right)}{\partial y'}\sin\theta_s\right\}\right]dx'dy' \quad (51)$$

4. VALIDATION OF ALGORITHM AND SCATTERING ANALYSIS

4.1. Validation of Algorithm

In order to verify the correctness and effectiveness of the SM-PB algorithm, the scattering coefficients of rough surfaces with large dielectric constants were calculated and compared with the results of the MoM algorithm, and the two result curves are plotted in Fig. 4.

It is found that the two curves match well, which indicates that the calculation results of the algorithm in this paper are correct, and it is effective to use it to study the scattering characteristics of rough surfaces. The parameters used in the calculation are: the side length of the square rough surface is $L = 12\lambda$; the root mean square height is $h = 0.2\lambda$; the correlation length is $l_x = l_y = 1.0\lambda$; the angle of incidence is $\theta_i = 30°$; the dielectric constant is $\varepsilon_{1r} = 40 + 20i$; the conical wave width is $g = 4\lambda$; the strong and weak correlation distance is $r_d = 3\lambda$; the dense profile density is $n_{dg} = 16$; and the sparse profile density is $n_{cg} = 4$.
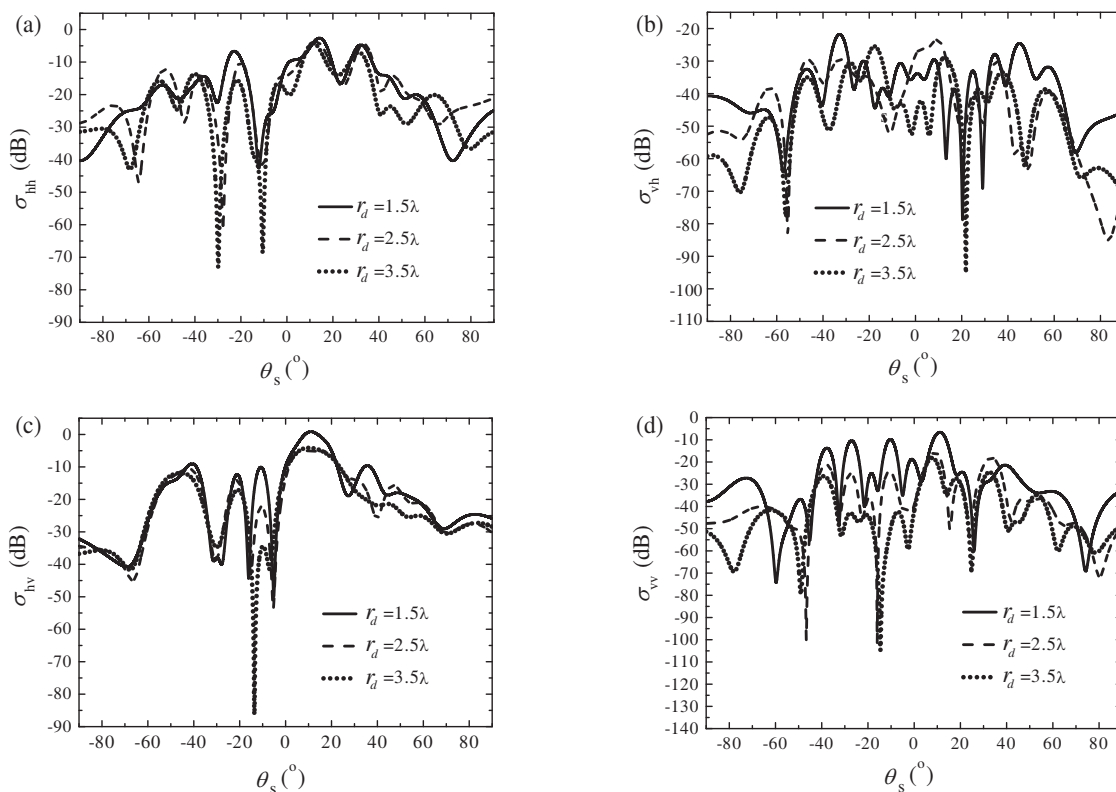
FIGURE 6. The variation curve of scattering coefficient with r_d. (a) hh polarization. (b) vh polarization. (c) hv polarization. (d) vv polarization.

TABLE 1. Comparison of computation time(s) between SM-PB and MoM.

	$N_1 = 600$	$N_2 = 1200$	$N_3 = 1800$	$N_4 = 2400$	$N_5 = 6000$
MoM	206	1131	3061	4998	7646
SM-PB	39	226	418	681	1076

The curve of simulation time (average time for 20 simulations) with r_d is given in Fig. 5. The computer configuration is: CPU Pentium(R) Dual-Core, main frequency 2.5 GHz, memory 2G. When r_d is small, the scattering from the far-field region of the rough surface takes up the major part and requires several iterations to achieve the required computational accuracy, leading to more time consumption. When r_d is relatively large, the scattering from the near-field accounts for the major part and is computationally intensive. Although the number of iterations decreases, the single calculation time increases, leading to an increase in the overall consumption time. Therefore, a reasonable choice of r_d value can improve the efficiency of the calculation to a certain extent. However, the optimal value of r_d is not fixed, is different for different rough surface parameters, and needs to be determined on a case-by-case basis.

To further prove the advantage of the algorithm in computational efficiency, we used SM-PB and MoM to calculate different sizes of rough surfaces (corresponding to different unknowns) and statistically analyzed their calculation times. In Table 1, we selected five examples, and the results show that compared with traditional MoM algorithms, the proposed algorithm significantly improves computational speed and sig-

nificantly saves calculation time. Additionally, the proposed algorithm requires relatively less computation time for calculating large-sized rough surfaces. These results indicate that the proposed algorithm has high computational efficiency and is capable of effectively handling rough surfaces of various sizes.

The parameters used in the calculation are: the side length of the square rough surface is $L_1 = 6\lambda$, $L_2 = 12\lambda$, $L_3 = 24\lambda$, $L_4 = 48\lambda$, $L_5 = 96\lambda$; the root mean square height is $h = 0.2\lambda$; the correlation length is $l_x = l_y = 1.0\lambda$; the angle of incidence is $\theta_i = 30°$; the dielectric constant is $\varepsilon_{1r} = 40 + 20i$; the conical wave width is $g = 4\lambda$; the strong and weak correlation distance is $r_d = 3\lambda$, the dense profile density is $n_{dg} = 16$; and the sparse profile density is $n_{cg} = 4$.

The scattering coefficients of the rough surface are calculated when r_d is 1.5λ, 2.0λ, 2.5λ, 3.0λ, 3.5λ, respectively, and their resultant curves are plotted in Fig. 6.

From these four plots, it can be seen that when r_d is different, the calculated scattering coefficient of the rough surface varies greatly, indicating that r_d has a great influence on the scattering coefficient. When r_d is smaller, the fluctuation of the curve is larger, and the degree of agreement with other curves is not very good, which indicates that the accuracy of the calculation is dif-
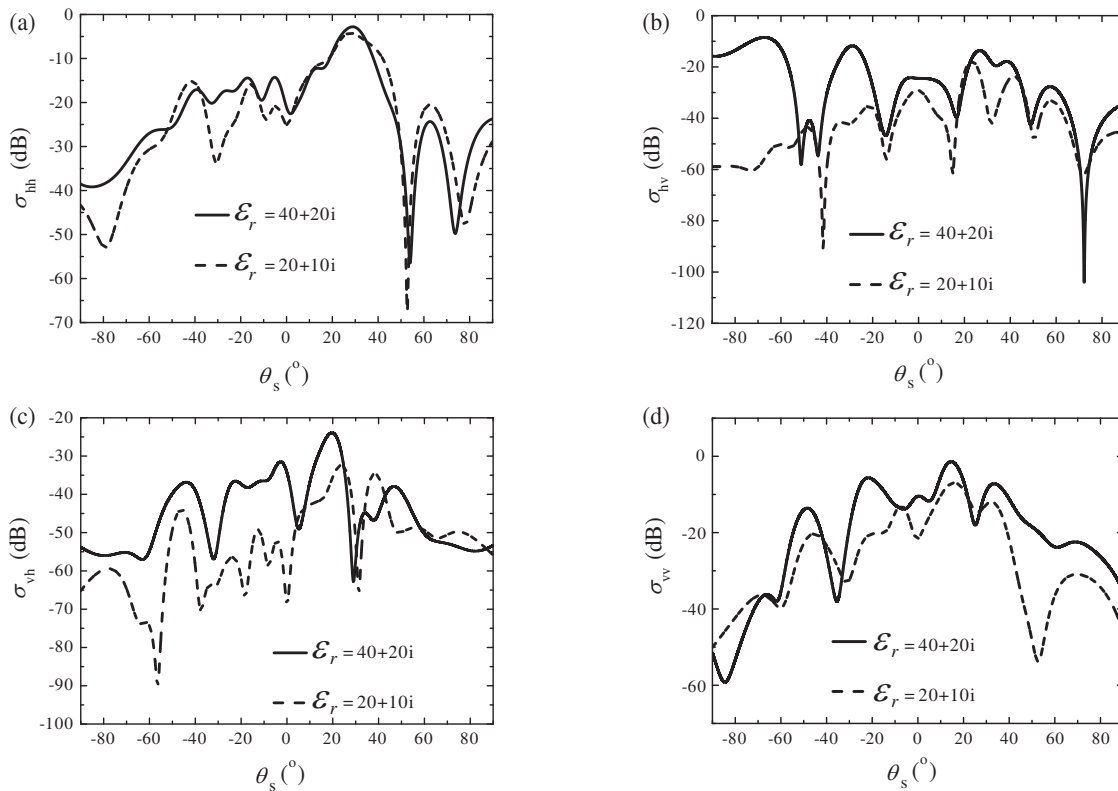
FIGURE 7. The variation curve of scattering coefficient with dielectric constant. (a) hh polarization. (b) hv polarization. (c) vh polarization. (d) vv polarization.

ficult to be guaranteed at this time. When r_d is larger than 2.5λ, the agreement of several curves at this time is better, which indicates that the accuracy of the calculation is higher.

The simulation results are consistent with the analysis of the algorithm: when the correlation distance is small, the near-field matrix only accounts for a small part of the matrix equations, and most of it is the far-field matrix, which requires several iterations to achieve the specified accuracy due to the low density of the far-field profiles. When the correlation distance is larger, the near-field matrix increases, and the proportion of the far-field matrix decreases. Due to the high density of near-field profiles, the amount of data to be computed increases, and although the convergence is better, the huge computational volume slows down the computational efficiency.

Combined with the observation in Fig. 5, it can be found that the choice of r_d is more reasonable when the value of it is taken as 2.5λ, considering the accuracy and efficiency of the algorithm. If the computation time is sufficient, and the accuracy of the algorithm is more important, consider increasing the value of r_d appropriately, and the results obtained will be accurate.

The parameters used in the calculation are: the strong and weak correlation distance is $r_{d1} = 1.5\lambda$, $r_{d2} = 2.5\lambda$, $r_{d3} = 3.5\lambda$; the side length of the square rough surface is $L = 12\lambda$; the root mean square height is $h = 0.2\lambda$; the correlation length is $l_x = l_y = 1.0\lambda$; the angle of incidence is $\theta_i = 30°$; the dielectric constant is $\varepsilon_{1r} = 40 + 20i$; the conical wave width is $g = 4\lambda$; the dense profile density is $n_{dg} = 16$; and the sparse profile density is $n_{cg} = 4$.

Figure 7 shows the variation curve of the scattering coefficient with dielectric constant, which mainly illustrates the effect of the dielectric constant of the rough surface on the scattering characteristics. As can be seen from the figure, in both cases, the scattering coefficient reaches a maximum near the specular direction. When the dielectric constant decreases, its specular scattering intensity decreases due to the weaker reflectivity of the radar beam at this time. In addition, it can be found that for larger dielectric constants, the backscattering is very strong and much larger than the backscattering for smaller dielectric constants, and this phenomenon is more obvious for hv and hv polarization modes, which reflects the larger the real part of the dielectric constant, the stronger the reflection, and the smaller the imaginary part, the larger the transmission and the smaller the reflection.

The parameters used in the calculation are: the root mean square height is $h_1 = 0.2\lambda$, $h_2 = 0.4\lambda$, and $h_3 = 0.6\lambda$; the strong and weak correlation distance is $r_d = 3\lambda$; the side length of the square rough surface is $L = 12\lambda$; the correlation length is $l_x = l_y = 1.0\lambda$; the angle of incidence is $\theta_i = 20°$; the dielectric constant is $\varepsilon_{1r} = 40 + 20i$; the conical wave width is $g = 4\lambda$; the dense profile density is $n_{dg} = 16$; and the sparse profile density is $n_{cg} = 4$.

To explore the specific impact of different root-mean-square heights on the scattering properties of rough surfaces, we set three sets of root-mean-square height parameters: $h_1 = 0.2\lambda$, $h_2 = 0.4\lambda$, and $h_3 = 0.6\lambda$. After precise calculations, we
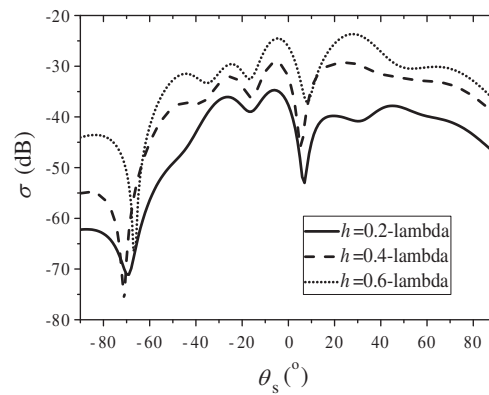
FIGURE 8. The impact of h on the scattering properties of rough surfaces.

obtained the corresponding scattering coefficients and plotted these data in Fig. 8.

As can be clearly seen from Fig. 8, in most directions, the scattering coefficient increases with the increase in roughness. This is because with the increase in roughness, the uneven areas on the rough surface increase, resulting in more incident light being scattered in various directions.

However, it is worth noting that the scattering coefficient exhibits a downward trend in the specular direction. This is mainly because in this particular direction, the energy of specular reflection dominates, while the received diffuse reflection energy is relatively small. Therefore, as the roughness increases, the energy of specular reflection also decreases accordingly, resulting in a decrease in the scattering coefficient.

In summary, the influence of root-mean-square height on the scattering properties of rough surfaces is complex. This includes both an increase in the scattering coefficient and a decrease in the specular direction. This finding is important for understanding and optimizing the scattering properties of rough surfaces.

5. CONCLUSION

In this paper, an accelerated SM-PB algorithm is proposed for the calculation of two-dimensional dielectric rough surfaces with large dielectric constants. Based on this algorithm, the electromagnetic scattering is calculated for different r_d and different dielectric constants, and it is found that the scattering is strong for large dielectric constants and much larger than the backward scattering for rough surfaces with small dielectric constants, and this phenomenon is more obvious in hv and hv polarization modes, reflecting that the larger the real part of the dielectric constant is, the stronger the reflection is. And the smaller the imaginary part is, the larger the transmission is and the smaller the reflection is. At the same time, in order to balance the accuracy and efficiency of the calculation, the value of r_d must be carefully considered; otherwise, it will lead to long calculation time or low calculation accuracy. The next step is to establish scattering models for different environments, calculate more environmental scattering examples, and study the electromagnetic scattering characteristics in different environments.

ADDITIONAL STATEMENTS

There are no conflicts of interest to disclose for all the authors.

REFERENCES

[1] Wagner, W., R. Lindorfer, T. Melzer, S. Hahn, B. Bauer-Marschallinger, K. Morrison, J.-C. Calvet, S. Hobbs, R. Quast, I. Greimeister-Pfeil, and M. Vreugdenhil, "Widespread occurrence of anomalous C-band backscatter signals in arid environments caused by subsurface scattering," *Remote Sensing of Environment*, Vol. 276, 113025, Jul. 2022.

[2] Li, J., M. Zhang, W. Jiang, and P. Wei, "Improved FBAM and GO/PO Method for EM Scattering Analyses of Ship Targets in a Marine Environment," *Sensors*, Vol. 20, No. 17, 4735, Sep. 2020.

[3] Bouchet, D., R. Carminati, and A. P. Mosk, "Influence of the local scattering environment on the localization precision of single particles," *Physical Review Letters*, Vol. 124, 133903, Apr. 2020.

[4] Li, J., M. Zhang, L. Wang, and Y. Jiao, "An efficient way for studying the em scattering from a marine environment with multiple ships," *IEEE Antennas and Wireless Propagation Letters*, Vol. 19, No. 9, 1526–1530, Sep. 2020.

[5] Jiang, J., X. Pan, and T. C. Yang, "Sparse reconstruction-based inverse scattering imaging in a shallow water environment," *IEEE Access*, Vol. 8, 180 305–180 316, 2020.

[6] DeCourcy, B. J. and T. F. Duda, "Mode coupling and scattering in a submarine canyon environment," *The Journal of The Acoustical Society of America*, Vol. 146, No. 4, 2887–2887, 2019.

[7] Gunderson, A., "Applying a numerical Green's function approach to scattering within complex seafloor environments," *The Journal of The Acoustical Society of America*, Vol. 146, No. 4, 2905–2906, 2019.

[8] Xue, W., Z. Chen, W. Tian, Y. Wu, and B. Hua, "A cascade defense method for multidomain adversarial attacks under remote sensing detection," *Remote Sensing*, Vol. 14, No. 15, Aug. 2022.

[9] Ma, T. J., "Remote sensing detection enhancement," *Journal of Big Data*, Vol. 8, No. 1, 1–13, Oct. 2021.

[10] Li, Z., Y. H. Hu, and F. Yan, "Feature analysis and extraction of complex motion target based on coherent laser remote sensing detection," *Advanced Materials Research*, Vol. 588, 1076–1080, 2012.

[11] Lv, P., Y. Tang, K. Liu, B. Zhang, S. Wang, and Y. Du, "Study CCD image motion for remote sensing detection," in *27th International Congress on High Speed Photography and Photonics*, Vol. 6279, No. 1-3, 1528–1534, Xian, China, Sep. 2007.

[12] Keder, J., M. Strizík, P. Berger, A. Cerny, P. Engst, and I. Nem-covaá, "Remote sensing detection of atmospheric pollutants by differential absorption LIDAR 510M/SODAR PA2 mobile system," *Meteorology and Atmospheric Physics*, Vol. 85, No. 1-3, 155–164, Jan. 2004.

[13] Zhou, C. B., W. G. Huang, J. S. Yang, F. Bin, H. G. Zhang, D. L. Li, A. Q. Shi, Q. M.Xiao, and X. L. Lou, "Remote sensing detection of complex oceanic features by using multi-parameter synthetic aperture radar (SAR)," in *Atmospheric and Oceanic Processes, Dynamics, and Climate Change*, Vol. 4899, 160–164, Oct. 2003.

[14] Liu, Z., "Radar image processing and simulation technology based on wavelet transform," *Basic & Clinical Pharmacology & Toxicology*, Vol. 128, No. 1, SI, 98, Jan. 2021.

[15] Liu, H., F. Pang, Z. Fu, and C. Liu, "Marine radar image processing of compressed sensing based on arbitrary block statistical histogram and dynamic dictionary," *IEEE Access*, Vol. 7, 57 383–57 398, 2019.

[16] Sumaiya, M. N. and R. S. S. Kumari, "SAR image despeckling using heavy-tailed Burr distribution," *Signal Image and Video Processing*, Vol. 11, No. 1, 49–55, Jan. 2017.

[17] Heymann, F., P. Banyś, and C. Saez, "Radar image processing and AIS target fusion," *TransNav: International Journal on Marine Navigation and Safety of Sea Transportation*, Vol. 9, No. 3, 443–448, 2015.

[18] Goller, A. and F. Leberl, "Radar image processing with clusters of computers," *IEEE Aerospace and Electronic Systems Magazine*, Vol. 24, No. 1, 18–22, Jan. 2009.

[19] Jin, J.-M., *The Finite Element Method in Electromagnetics*, John Wiley & Sons, 2015.

[20] Taflove, A. and S. C. Hagness, *Computational Electrodynamics: The Finite-Difference Time-Domain Method*, Artech House, 2005.

[21] Yee, K., "Numerical solution of initial boundary value problems involving Maxwell's equations in isotropic media," *IEEE Transactions on Antennas and Propagation*, Vol. 14, No. 3, 302–307, 1966.

[22] Harrington, R. F., *Field Computation by Moment Methods*, Macmillan Company, 1968.

[23] Dölz, J., "A higher order perturbation approach for electromagnetic scattering problems on random domains," *SIAM/ASA Journal on Uncertainty Quantification*, Vol. 8, No. 2, 748–774, 2020.

[24] Ozgun, O., R. Mittra, and M. Kuzuoglu, "A novel CEM technique for modeling electromagnetic scattering from metasurfaces," *International Journal of Numerical Modelling: Electronic Networks, Devices and Fields*, Vol. 33, No. 2, e2681, Mar. 2020.

[25] He, W., X. Weng, W. Luo, H. Chen, X. Wu, K. Li, Y. Huang, and B. Liu, "Modeling of camouflage grass and the calculation of its electromagnetic scattering characteristics," *IEEE Access*, Vol. 8, 45 033–45 040, 2020.

[26] Pan, G. W., *Wavelets in Electromagnetics and Device Modeling*, John Wiley & Sons, 2003.

[27] Braunisch, H., Y. Zhang, C. O. Ao, S. E. Shih, Y. E. Yang, K. H. Ding, J. A. Kong, and L. Tsang, "Tapered wave with dominant polarization state for all angles of incidence," *IEEE Transactions on Antennas and Propagation*, Vol. 48, No. 7, 1086–1096, Jul. 2000.